

Date of publication xxxx 00, 0000, date of current version xxxx 00, 0000.

Digital Object Identifier xxxxx

Fusion of Visual-Inertial Odometry with LiDAR Relative Localization for Cooperative Guidance of a Micro-Scale Aerial Vehicle

VÁCLAV PRITZL¹, MATOUŠ VRBA¹, PETR ŠTĚPÁN¹, and MARTIN SASKA¹, (Member, IEEE)

¹Multi-robot Systems Group, Department of Cybernetics, Faculty of Electrical Engineering, Czech Technical University in Prague, Technická 2, Prague, 166 27, Czech Republic

Corresponding author: Václav Pritzl (e-mail: vaclav.pritzl@fel.cvut.cz).

This work was funded by CTU grant no SGS23/177/OHK3/3T/13, by the Czech Science Foundation (GAČR) under research project no. 23-07517S, and by the European Union under the project Robotics and advanced industrial production (reg. no. CZ.02.01.01/00/22_008/0004590).

arXiv:2306.17544v3 [cs.RO] 28 Jan 2026

ABSTRACT A novel relative localization approach for guidance of a micro-scale Unmanned Aerial Vehicle (UAV) by a well-equipped aerial robot fusing Visual-Inertial Odometry (VIO) with Light Detection and Ranging (LiDAR) is proposed in this paper. LiDAR-based localization is accurate and robust to challenging environmental conditions, but 3D LiDARs are relatively heavy and require large UAV platforms, in contrast to lightweight cameras. However, visual-based self-localization methods exhibit lower accuracy and can suffer from significant drift with respect to the global reference frame. To benefit from both sensory modalities, we focus on cooperative navigation in a heterogeneous team of a primary LiDAR-equipped UAV and a secondary micro-scale camera-equipped UAV. We propose a novel cooperative approach combining LiDAR relative localization data with VIO output on board the primary UAV to obtain an accurate pose of the secondary UAV. The pose estimate is used to precisely and reliably guide the secondary UAV along trajectories defined in the primary UAV reference frame. The experimental evaluation has shown the superior accuracy of our method to the raw VIO output, reaching the average 3D Absolute Trajectory Error (ATE) of 0.28 m, and demonstrated its capability to guide the secondary UAV along desired trajectories while mitigating VIO drift. Thus, such a heterogeneous system can explore large areas with LiDAR precision, as well as visit locations inaccessible to the large LiDAR-carrying UAV platforms, as was showcased in a real-world cooperative mapping scenario.

INDEX TERMS Cooperative guidance, LiDAR, localization, mobile robots, multi-robot system, unmanned aerial vehicle, visual-inertial odometry.

MULTIMEDIA ATTACHMENT

<http://mrs.felk.cvut.cz/coop-fusion>

I. INTRODUCTION

Autonomous multi-rotor Unmanned Aerial Vehicles (UAVs) are well-suited for emergency response and Search and Rescue (SAR) tasks in confined indoor spaces. In these applications, the UAVs operate in Global Navigation Satellite System (GNSS)-denied environments but still require accurate positioning in a world reference frame, e.g., to precisely report victim positions, as was demonstrated in the Defense Advanced Research Projects Agency (DARPA) Subterranean (SubT) challenge [1], [2].

Camera-equipped UAVs can be localized by Visual-Inertial Odometry (VIO) techniques and may be small enough to

fly through highly confined environments. However, visual-based localization approaches are heavily dependent on lighting conditions [3], the amount of texture in the environment [4], and suffer from long-term drift with respect to the world frame due to the VIO's four unobservable Degrees of Freedom (DOFs) [5]. Monocular camera-based methods exhibit scale unobservability under constant acceleration [6], [7]. The impracticality of purely vision-based approaches for indoor and subterranean SAR missions was confirmed by all DARPA SubT teams, including the team of authors of this article.

Light Detection and Ranging (LiDAR)-based methods rely on the geometric structure of the environment. In comparison to visual-based methods, 3D LiDAR-based localization exhibits lower drift and performs well under challenging light-

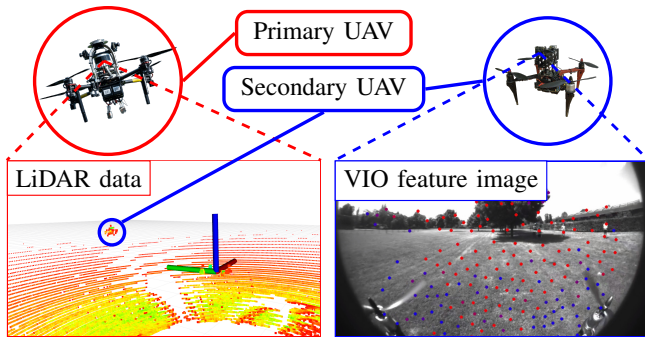


FIGURE 1. The primary UAV carrying a 3D LiDAR guides the secondary camera-equipped UAV using a fusion of LiDAR detections and VIO data.

ing conditions. Most of the best-performing algorithms on the Karlsruhe Institute of Technology and Toyota Technological Institute (KITTI) dataset [8] are LiDAR-based. However, 3D LiDARs are relatively heavy and power-consuming. Although all the teams in the DARPA SubT challenge relied on LiDARs, the UAV platforms needed for carrying such payloads were too bulky for exploring many narrow passages [9].

Using teams of UAVs with different sensors keeps the benefits of the localization methods while mitigating the disadvantages. The LiDAR-equipped UAV can share its localization data and information about the surrounding environment with the lightweight UAVs. The camera-equipped UAV can pass through more confined spaces and cheaply extend the perception range of the UAV team due to its low cost.

We propose a novel approach to cooperative flight in GNSS-denied environments, providing accurate relative localization between the UAVs, and enabling direct guidance of less-capable UAVs by a more-capable UAV, mitigating the effects of localization drift. We focus on the case of a primary UAV utilizing 3D LiDAR-based Simultaneous Localization and Mapping (SLAM) and a lightweight secondary UAV carrying a monocular camera utilizing VIO (see Fig. 1).

The proposed approach can enable a variety of multi-UAV tasks in GNSS-denied environments, e.g., cooperative exploration and mapping in confined, sensory-degraded spaces or correcting VIO drift of a cooperating team of micro-UAVs.

A. NOTATIONS

We denote vectors as bold lowercase letters, matrices as bold upright uppercase letters, and reference frames as simple uppercase letters. Let ${}^B_A \mathbf{t}$ be the vector describing the position of the origin of frame A in frame B . Let ${}^B_A \mathbf{R} \in SO(3)$ be the rotation matrix from frame A to frame B . We denote

$${}^B_A \mathbf{T} = \begin{bmatrix} {}^B_A \mathbf{R} & {}^B_A \mathbf{t} \\ \mathbf{0}^T & 1 \end{bmatrix} \in SE(3) \quad (1)$$

as the transformation matrix from frame A to frame B . Let ${}^A \mathbf{x}_{[t_k]}$ be a 3D position vector in frame A at time t_k . We denote ${}^A D$ as the set of LiDAR detections in reference frame A and ${}^A \chi$ as the desired UAV trajectory in frame A .

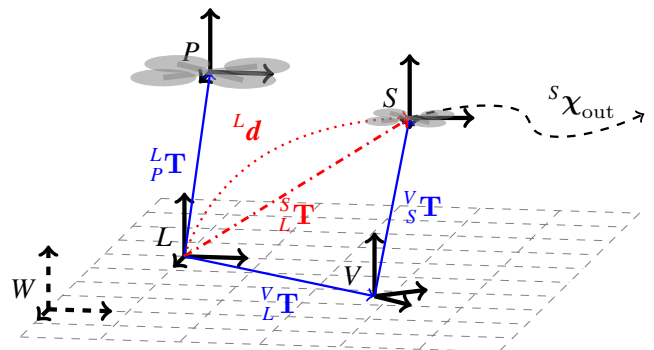


FIGURE 2. W is the world reference frame. Frames P and S correspond to the primary and secondary UAV, respectively. The primary UAV is localized by LiDAR SLAM in the local frame L , while the secondary UAV is localized by VIO in the local frame V . The origins of frames L , V are at the poses where the algorithms were initialized. Frames L and V have 4 unobservable DOFs w.r.t. W , resulting in long-term drift. Frame V suffers from significantly larger drift than frame L . ${}^L d$ is position of the secondary UAV detected from LiDAR data. The reference for the secondary UAV's movement is given in the frame L , transformed to ${}^S \chi_{out}$ using the relative localization, and transmitted to the secondary UAV.

B. PROBLEM STATEMENT

We focus on tight cooperation in a heterogeneous UAV team with various localization sensors. The crucial part is fusing LiDAR relative localization with VIO ego-motion estimates for guidance of a less-capable UAV by a more-capable UAV. The more-capable *primary* UAV carries a 3D LiDAR and is subject to small long-term localization drift. The less-capable *secondary* UAV is equipped with a monocular camera and suffers from significantly larger long-term localization drift. Both UAVs carry an onboard computer, a wireless communication module, a Flight Control Unit (FCU) with an embedded attitude controller, and an Inertial Measurement Unit (IMU). The UAVs operate in a GNSS-denied environment. All algorithms run fully on board the UAVs.

The problem is illustrated in Fig. 2. The first task is to estimate the transformation ${}^V_L \mathbf{T}$ between the LiDAR SLAM frame L and VIO frame V and the transformation ${}^S_L \mathbf{T}$ between L and the secondary UAV body frame S to provide relative localization between the UAVs. All reference frames are aligned with the gravity vector obtained from the IMU data. Given general motion, VIO always has four unobservable directions, corresponding to the global translation and global yaw. As reported in [6], monocular VIO additionally exhibits scale unobservability under constant acceleration and global orientation unobservability when the UAV is not rotating. The scale unobservability under constant acceleration will manifest as long-term drift in the global x, y, z translation of the output. While the global orientation unobservability given no rotation can cause short-term drift in the direction of the estimated gravity vector, the drift will be corrected once the robot rotates again. In practice, we assume general rotating motion of the UAV, as the UAV needs to change its tilt even to perform a translational motion, to compensate for wind disturbances while hovering, etc. Therefore, we assume only negligible short-term drift in the gravity vector with quick

corrections back to the correct global values. Therefore, we estimate 4-DOF transformations, consisting of 3D translation and relative heading.

The second task is to use the relative localization data to guide the secondary UAV along the desired trajectory ${}^L\chi_{in}$, defined in the LiDAR SLAM reference frame L . The aim is to: 1) give the primary UAV the capability to directly guide the secondary UAV to, e.g., inspect a specific place or pass around obstacles, 2) mitigate the effects of VIO drift to approach the trajectory tracking precision achievable with the less-drifting primary UAV localization.

Depending on the environment, the LiDAR relative localization output Ld is subject to potential false detections and variable delay due to LiDAR data processing time. The communication between the UAVs is subject to variable delay depending on the network reliability. We assume no prior knowledge about the transformation V_LT or about the initial UAV poses. The proposed approach tries to minimize the computational and payload requirements on the secondary UAV by offloading them onto the primary UAV.

C. RELATED WORK

1) UAV relative localization

In unknown GNSS-denied environments, there are several ways to solve relative localization between UAVs. Marker-based visual detectors utilize markers, such as ultraviolet (UV) LEDs, in combination with UV-sensitive cameras [10]. Marker-less visual approaches typically rely on a Convolutional Neural Network (CNN) [11]–[14]. In [15], the authors proposed a visual relative localization method for large UAV swarms, estimating the density of UAVs over distance rather than the positions of individual UAVs. However, machine learning-based techniques are susceptible to changes in the appearance of the targets and the environment. In [16], the authors proposed a UAV detection method from event camera streams based on detecting the spinning propellers. In [17], a motion-guided approach for detecting small UAVs in complex and non-planar scenes was proposed, combining motion feature enhancement, multi-target tracking, and an appearance-based classifier. The authors of [18] proposed a keypoint-guided method for estimating the 6-DOF pose of a target UAV from monocular camera data, relying on known dimensions of the target UAV. Although this field of research is progressing, vision-based approaches often struggle under low visibility and fail to provide precise 3D position estimates due to inaccurate distance estimation [12], as the approaches require a priori knowledge about the UAV's physical size to estimate the 3D distance from the camera. Such a priori information may be provided directly or encoded in the neural network using the training dataset. In [19], the authors proposed an active localization correction approach relying on visual detections. The approach used a CNN for detection of cooperating UAVs, combined with measurements from a depth camera, and focused on controlling the yaw of the UAVs to balance between obtaining relative localization data and observing the environment. The limited Field Of View

(FOV) of the cameras is a significant drawback of visual-based methods. In contrast, many 3D LiDARs, such as the one used in our approach, have full 360° horizontal FOV, removing the need to rotate the UAV or to use multiple cameras. Furthermore, in practice, the depth cameras have a usable range of a few meters, compared to tens of meters in the case of the LiDAR sensors.

Equipping the UAVs with Ultra-wideband (UWB) modules provides distance measurements between pairs of the modules [20]. The overall localization accuracy is highly dependent on the shape and size of the UAV formation, as it may suffer from unobservabilities and dilution of precision.

A multi-robot SLAM method can obtain the relative poses through map merging and inter-robot loop closures, utilizing, e.g., LiDAR data [21], [22], stereo camera data [23], or monocular camera data [24]. Such approaches require data of comparable modalities to perform the place recognition / loop closures. However, LiDAR and visual data use inherently different types of data, as LiDAR data provides information about the geometric structure of the environment, while visual data provides visual features. Depending on the environment, it may be difficult or even impossible to perform reliable place recognition based on these different sensory modalities. Furthermore, such approaches require communicating significant amounts of data or making compromises between the amount of shared data and contained information, influencing the accuracy of the localization [25]. Often, they use a ground station for computations, but we aim to run everything on board the computationally-constrained UAV platforms. Our method enables efficient relative localization between heterogeneous UAVs without requiring any place recognition, high-bandwidth data transmission, or ground-station computation.

3D LiDAR data can be used for direct detection of cooperating robots. In [26], a fusion of 3D LiDAR, fisheye camera, and UWB data was used for tracking a UAV flying above a LiDAR- and camera-equipped Unmanned Ground Vehicle (UGV), with the UAV wirelessly sharing IMU and 1D LiDAR data. In [27], [28], a decentralized LiDAR-inertial swarm odometry was proposed, utilizing direct detections of cooperating UAVs from reflectivity values of LiDAR data. However, these methods tightly couple LiDAR data across the swarm, which prevents heterogeneous configurations and requires heavy, power-demanding, and costly 3D LiDARs on every UAV. By contrast, our approach enables a primary LiDAR-equipped UAV to cooperate with a secondary, lightweight camera-based UAV, significantly reducing size, weight, and power requirements for the secondary vehicle.

In this paper, we utilize direct detections of UAVs from LiDAR data, taking advantage of the robustness of the LiDAR sensor and of the ability to easily obtain precise 3D positions of the cooperating UAVs. The approach is based on our previous work on detection of intruder UAVs from LiDAR data [29], [30] and can work without markers or with optional reflective markers aiding the detection process in cluttered environments. We would like to refer the reader to [30] for a thorough analysis of the LiDAR-based detection method, in-

cluding comparisons with other methods for UAV detection.

2) Cooperative navigation improving UAV localization

Our approach is similar to methods for improving localization in GNSS-challenging environments, where UAVs with reliable GNSS-based localization share data with another UAV in a GNSS-challenging area [31], [32]. These approaches utilized visual tracking for relative localization.

Using the relative localization data, we aim to improve the navigation performance of a UAV utilizing visual-based self-localization. Such a goal can be achieved by fusion with UWB measurements. For a single-UAV case, a fusion of data from static UWB anchors, LiDAR odometry, IMU, and VIO was proposed in [33]. However, placing static UWB anchors in the area is not viable in an emergency scenario. The use of multiple robots, each carrying a UWB module, decreases the dependence on external infrastructure. Such approaches fusing UWB and VIO were proposed in [34] for collaborative localization of two UAVs and in [35] for distributed formation estimation in large UAV swarms. As previously mentioned, UWB modules provide only distance measurements between each pair of devices, and thus the accuracy of such a solution heavily depends on the shape of the UAV formation. In a two-UAV team such as ours, UWB alone provides only one DOF per link, while a single LiDAR detection provides three DOFs, fully constraining the relative 3D position.

In [36], the authors fused the detections from a CNN with UWB data and VIO for relative localization in a UAV swarm. The same authors fused map-based inter-UAV loop-closures in [37]. To obtain loop closures, the individual robots need to observe the environment in similar modalities and exchange the data, increasing communication demands. Thus, loop closures are not suitable for our heterogeneous UAV team. Zhang *et al.* [38] fused active visual-based relative localization with UWB and VIO data for formation control of a marker-equipped UAV swarm. However, such visual-based methods are not robust enough for the target emergency response and SAR tasks, which motivate our research. The authors of [39] focused on collaborative localization of a UGV-UAV team. Their approach relied mainly on UWB and VIO data, with 3D LiDAR detections utilized during initialization. In contrast, our approach does not require any UWB modules and we utilize the precise 3D positions obtained from the LiDAR data during the entire localization process.

The authors of [40] utilized a heterogeneous team of LiDAR-carrying UGVs and camera-equipped UAVs with the goal of detecting the UGVs from onboard cameras on UAVs and using them as landmarks for improving the UAV localization. Their work focused mainly on the optimal placement of the UGVs in the environment. In contrast, we focus on a heterogeneous UAV-only team with the LiDAR-carrying UAV detecting the camera-equipped UAV. Relative localization in a UAV team requires obtaining their 3D positions very accurately and 3D LiDAR sensors represent an ideal choice for such a task.

3) VIO drift mitigation

In [41], VIO drift was mitigated by finding feature correspondences in VIO data and prior LiDAR maps. Our approach does not require prior maps and can be deployed in previously unseen environments. In GNSS-enabled environments, VIO drift can be corrected by fusing raw Doppler velocities and pseudoranges [42] or 3D GNSS positions [43]. In [43], the authors obtained the GNSS-VIO frame transformation using window-based optimization and transformed the VIO state to the GNSS frame during initialization to avoid unobservabilities. The GNSS data are in the global frame but suffer from short-term meter-level drift. LiDAR data are in a local frame, resulting in minor long-term drift w.r.t. global frame, but exhibit centimeter-level precision. Our approach uses window-based optimization not only for initialization but during the entire estimation process.

In [44], [45], the authors focused on VIO and visual target tracking, improving the performance of both thanks to their tight coupling. We instead improve the navigation performance of a VIO-using UAV by guiding it by another UAV with less-drifting localization. We opted for a loosely-coupled approach to mitigate issues with modeling errors hurting the performance, which can be more pronounced in a tightly-coupled estimator [45], and to enable our approach to be universally usable with any VIO algorithm.

4) Contributions

The proposed relative localization method can accurately obtain 3D positions of UAVs without prior knowledge of their size. It is robust to low illumination due to the nature of the LiDAR sensor and does not require any additional hardware apart from the 3D LiDAR that is simultaneously used for the ego-localization of the primary UAV. Our approach poses minimal requirements on the secondary UAV, making the method compatible with a number of commercially-available UAVs and state-of-the-art VIO algorithms. It requires no prior information about the initial UAV poses. It is worth mentioning that the proposed approach is not limited to the use of VIO algorithms on board the secondary UAV, but can be easily applied to any odometry method providing localization data in some local reference frame thanks to its loosely-coupled nature.

The approach proposed in this paper is an extension of our previous work on utilizing 3D LiDAR detections to guide a cooperating UAV [46]. In this paper, we extend the relative localization approach by fusing the LiDAR detections with the VIO output, thus obtaining relative orientation between the UAVs and enabling to guide the secondary UAV along target trajectories with a variable desired heading. Simultaneously, the fusion approach removes the need for any a priori knowledge about the UAV poses. The proposed method has been used to enable subsequent research [47] on cooperative guiding of drones in cluttered environments [48] and cooperative indoor exploration [49]. Note that the aforementioned publications do not focus on the fusion of VIO with LiDAR relative localization but utilize the method proposed in this

paper for higher-level tasks enabled by this approach. The short workshop paper [47] provides only a high-level summary of these methods and their uses, without any details.

To the best of our knowledge, the proposed approach is the first solution to relative localization between heterogeneous UAVs based on LiDAR and VIO fusion. The key contribution of our work is to fuse the complementary strengths of LiDAR (accuracy, robustness to environmental conditions) and cameras (low weight, size, cost, and power demand) in a single heterogeneous UAV team. As shown in the experimental evaluation, such a setup provides accurate localization between the UAVs and enables precise guidance of the secondary UAV with drifting VIO. In a practical application, the proposed approach can be employed for guiding less-capable UAVs with minimal sensory payload through areas of visual sensory degradation.

The contributions of this work can be summarized as:

- A novel approach to UAV relative localization based on the fusion of LiDAR and VIO ego-motion data, which provides a common reference frame for a team of heterogeneously localized UAVs. Unlike existing solutions that rely on homogeneous sensors or lower-accuracy modalities, our approach leverages the high precision of 3D LiDAR to achieve accurate relative localization. The proposed method enables accurate estimation of the time-varying relative transformation between the different reference frames of the UAVs, and is able to quickly react to the coordinate frame drift while taking into account possible false detections and measurement delays.
- A cooperative guidance strategy utilizing the relative localization that allows the secondary UAV to track desired trajectories defined in the primary UAV reference frame while mitigating VIO drift.
- The raw data from our real-world experiments have been released online to provide a unique dataset useful for experimental verification of such relative localization approaches to the research community.

II. COOPERATIVE LOCALIZATION AND GUIDANCE APPROACH

The overall architecture of the proposed approach (see Fig. 3) is based upon the results of our preliminary work [46], which assessed the feasibility of using raw LiDAR detections to guide a cooperating UAV to desired positions. The UAV pair forms a closed feedback loop controlling the secondary UAV pose in the frame L . High-level planning and estimation run on board the primary UAV. The secondary UAV receives the desired trajectories ${}^S\chi_{\text{out}}$ and tracks references in its local frame V . The UAV pair is time-synchronized over the wireless network. This paper focuses mainly on the *UAV guider* module (see Fig. 4). The control pipeline used for tracking references in the local frames of each self-localization method is provided by the MRS UAV System [50]¹.

¹https://github.com/ctu-mrs/mrs_uav_system

A. LIDAR-BASED DETECTOR

The *LiDAR-based detector* performs multi-target detection and tracking of flying objects in the 3D LiDAR point clouds in frame L . The LiDAR data processing is based on our work on autonomous interception of intruder UAVs [29], [30].

The detector constructs a voxel-based occupancy map of the surrounding environment from LiDAR data and detects flying objects in the map. A Kalman filter-based point cluster-tracking approach is utilized to compensate for the uncertainty in the sensory data and mitigate delays caused by the processing time of the detection algorithm. Here, we describe the differences employed for its use in the proposed cooperative localization and guidance approach and encourage the reader to look into [30] for more details about the *LiDAR-based detector* itself, including its extensive experimental evaluation.

The *LiDAR-based detector* additionally receives the estimated UAV position ${}^L_s\mathbf{x}$ from the *UAV guider* module. The position is used in cluster-to-target association instead of the tracked target position if ${}^L_s\mathbf{x}$ is located within a desired uncertainty radius from a tracked target. The position ${}^L_s\mathbf{x}$ can be more accurate due to the incorporation of the low-delay VIO data.

The detected UAV can be optionally equipped with reflective markers to improve the detection robustness in cluttered environments. If the reflective markers are used, the detector processes reflectivity information contained in the LiDAR point cloud and discards point clusters that do not contain points above a predefined reflectivity threshold. When the reflective markers are used, the accuracy of the detections themselves stays the same, as the detections are produced by calculating the centroids of the original LiDAR clusters. The same LiDAR points would be used in the marker-less variation of the method. The reflective markers are passive. They only reflect incoming LiDAR beams and do not require any power source on board the UAV, unlike, e.g., the UV-based markers of [10]. The advantages of the use of reflective markers are:

- They provide an additional safety feature in cluttered environments. Although their use is not strictly necessary, it may be a desirable safety feature depending on the objects in the environment. For example, imagine a ceiling light hanging on a thin cable. Depending on the parameters of the LiDAR and the distance from the light, the LiDAR may not observe the cable in the LiDAR data, and the light will therefore appear to be a flying object, easily mistaken for a UAV. If the actual secondary UAV flies close to the ceiling light, the false detection may be falsely associated with the UAV, especially in the presence of VIO drift.

Disadvantages of the reflective markers:

- The reflective markers need to be placed on the UAV, requiring a slight modification of the UAV in comparison to the marker-less method. Since we assume cooperating

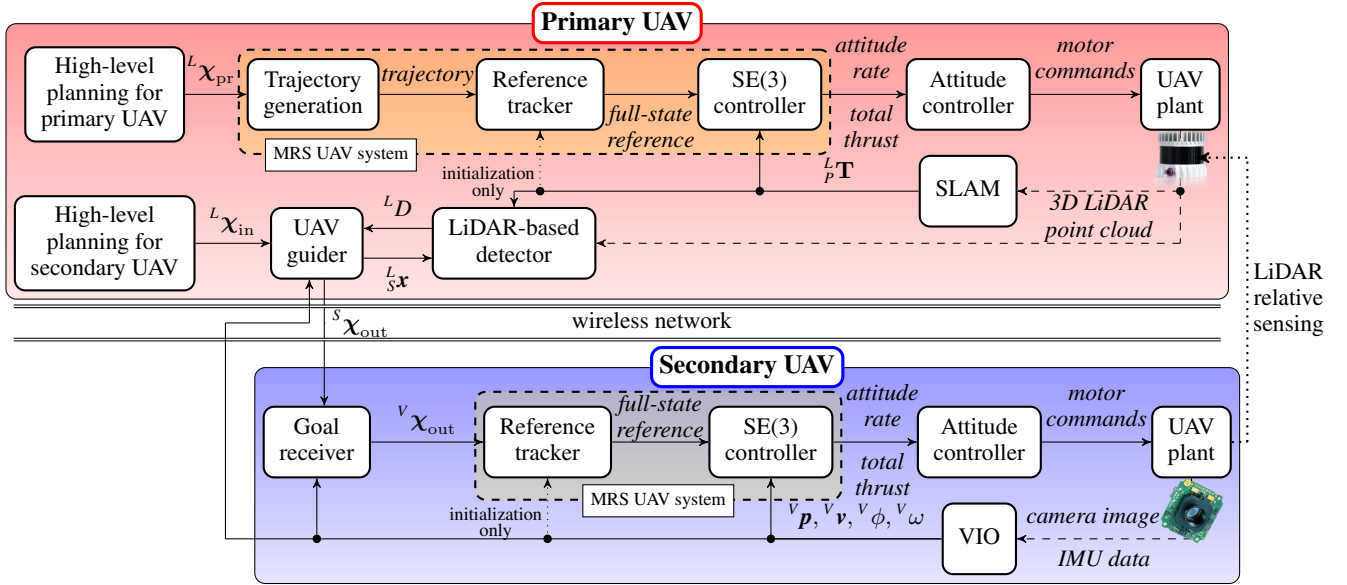


FIGURE 3. The primary UAV tracks the pose of the secondary UAV from the fusion of LiDAR and VIO data and transmits commands to the secondary UAV over a wireless network. Movement of the UAV pair is planned on board the primary UAV. Position control in the frame of each respective self-localization method is provided by the MRS UAV System [50].

UAVs (unlike in [30]), this is not a limitation of the proposed approach.

- If the reflective marker is too small and is not observed in the LiDAR data, correct UAV detections may be discarded. Such a situation may happen depending on the parameters of the LiDAR, i.e., on the spread between the LiDAR beams, on the distance between the UAVs, and on the size of the reflective markers.

Based on the presented advantages and disadvantages, the reflective markers are not necessary in open areas, but are an important safety feature in cluttered environments.

The detected 3D positions of all tracked objects are sent to the *UAV guider module* in the set of detections ${}^L D$.

B. UAV GUIDER

The *UAV guider* (see Fig. 4) estimates the transformation ${}^S_L T$ from the LiDAR detections and VIO data, and transforms the desired trajectories to the secondary UAV's frame S . The UAV pose is estimated in two loosely-coupled steps. The *Non-linear Least Squares (NLS)-based estimator* aligns LiDAR detections and VIO poses in a sliding window to produce ${}^V_L T$. The transformation ${}^V_L T$ connects the reference frames but lags behind the true transformation values in areas with large VIO drift. Therefore, the *Linear Kalman Filter (LKF)-based tracker* utilizes ${}^V_L T$ and fuses the latest LiDAR detections and VIO to provide a drift-compensated estimate of ${}^S_L T$ usable for transformation of the desired trajectories. The *LKF-based tracker* also deals with measurement delays and provides association of LiDAR detections based on their Mahalanobis distance.

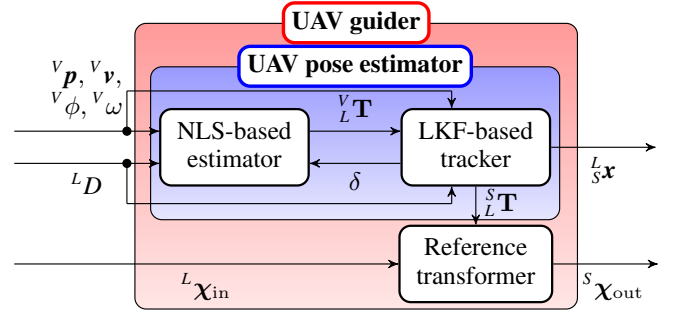


FIGURE 4. The UAV guider module fuses LiDAR detections with VIO data to estimate 4-DOF poses of the secondary UAV. The estimation result is used for transformation of references to the coordinate frame of the secondary UAV.

1) NLS relative transformation optimization

The 4-DOF transformation between the LiDAR SLAM frame L and the VIO frame V is defined as

$${}^V_L T = \begin{bmatrix} {}^V_L R(\theta) & {}^V_L t \\ \mathbf{0}^T & 1 \end{bmatrix} \in SE(3). \quad (2)$$

The problem of estimating its parameters from a set of LiDAR-VIO pose correspondences in a sliding window can be formulated as

$${}^V_L \hat{t}, \hat{\theta} = \arg \min_{{}^V_L t, \theta} \frac{1}{2} \sum_i \rho \left(\left\| {}^V_L R(\theta) {}^L d_{[t_i]} + {}^V_L t - {}^V p_{[t_i]} \right\|^2 \right), \quad (3)$$

$${}^V_L t \in \mathbb{R}^3, \theta \in [-\pi, \pi], \quad (4)$$

where ${}^V_L t$ is the relative translation vector between the reference frames, θ is the relative heading, ${}^L d_{[t_i]}$ is the LiDAR detection position at time t_i , and ${}^V p_{[t_i]}$ is the corresponding VIO position. $\rho(\cdot)$ denotes the loss function used for reducing

the influence of outliers on the optimization solution. In the experimental evaluation of the proposed approach, the Levenberg-Marquardt algorithm, implemented in the Ceres Solver [51], was employed for solving the NLS problem. The soft L1 loss function, defined as

$$\rho(s) = 2(\sqrt{1+s} - 1), \quad (5)$$

was employed, and the automatic differentiation functionality of the Ceres Solver was used to solve the problem.

The length of the sliding window is constant and predefined. The formulation of the optimization problem assumes constant ${}^L\mathbf{T}$ over the course of the sliding window. The LiDAR detections exhibit high accuracy with little long-term drift. The VIO positions exhibit significant long-term drift, especially in texture-less environments. Therefore, a longer window does not necessarily equal a better estimate. The window length must balance between measurement noise mitigation and long-term drift tracking. The optimal length selection may change with the environment, e.g., in an environment with a lot of features and little VIO drift, the window can be longer, whereas in a featureless environment with significant VIO drift, a shorter window is desired.

The LiDAR-VIO correspondence set $\left\{ \left[{}^L\mathbf{d}_{[t_i]}, {}^V\mathbf{p}_{[t_i]} \right]_i \right\}$ is constructed from the VIO position buffer by linearly interpolating the LiDAR detections to time stamps corresponding to each VIO position in the buffer. The result of the NLS optimization is only used if the optimization converges and its final cost is lower than a predefined threshold.

2) LKF-based tracker

The LKF-based tracker predicts the state of the secondary UAV in the frame L and outputs the estimated UAV position ${}^L\mathbf{x}$ and matrix ${}^L\mathbf{T}$ used for transforming the desired references for secondary UAV.

The tracker is based on an LKF with a recalculating history buffer [52]. The history buffer contains recent measurements and measurement covariance matrices sorted by time stamps. When the tracker predicts its state at a specific time, it is calculated using information from the oldest element in the buffer up to the desired time stamp. The tracker is based upon a 4-DOF constant-velocity model with a state vector

$$\mathbf{x}^{\text{KF}} = \left[{}^L\mathbf{x}^{\text{T}} \quad {}^L\mathbf{v}^{\text{T}} \quad {}^L\phi \quad {}^L\omega \right]_{8 \times 1}^{\text{T}}, \quad (6)$$

where ${}^L\mathbf{x}$ is the 3D position of the secondary UAV in the LiDAR SLAM frame, ${}^L\mathbf{v}$ is the velocity of the UAV, ${}^L\phi$ is the heading, and ${}^L\omega$ is the heading rate.

The state covariance matrix can be expressed as

$$\Sigma^{\text{KF}} = \begin{bmatrix} \Sigma_{xx} & \Sigma_{xv} & 0 & 0 \\ \Sigma_{vx} & \Sigma_{vv} & 0 & 0 \\ 0 & 0 & \Sigma_{\phi\phi} & \Sigma_{\phi\omega} \\ 0 & 0 & \Sigma_{\omega\phi} & \Sigma_{\omega\omega} \end{bmatrix}. \quad (7)$$

To achieve consistent performance when fusing unsynchronized measurements, the state covariance matrix is propagated forward in time at each prediction step using a

continuous-time representation with zero-mean white noise on linear velocity and heading rate [53]. The linear position and velocity submatrices from time t_k are propagated to time t_{k+1} based on the noise vector σ_v^2 as

$$\Sigma_{vv[t_{k+1}]} = \Sigma_{vv[t_k]} + \sigma_v^2 \Delta t \quad (8)$$

$$\Sigma_{xv[t_{k+1}]} = \Sigma_{xv[t_k]} + \Sigma_{vv[t_k]} \Delta t + \sigma_v^2 \frac{\Delta t^2}{2} \quad (9)$$

$$\Sigma_{vx[t_{k+1}]} = \Sigma_{vx[t_k]} + \Sigma_{vv[t_k]} \Delta t + \sigma_v^2 \frac{\Delta t^2}{2} \quad (10)$$

$$\Sigma_{xx[t_{k+1}]} = \Sigma_{xx[t_k]} + 2\Sigma_{xv[t_k]} \Delta t + \Sigma_{vv[t_k]} \Delta t^2 + \sigma_v^2 \frac{\Delta t^3}{3}, \quad (11)$$

where

$$\Delta t = t_{k+1} - t_k. \quad (12)$$

The heading and heading rate submatrices are updated analogously using the heading rate noise variance σ_ω^2 . The linear velocity noise is assumed to be isotropic, thus the process noise depends only on the parameters σ_v^2 and σ_ω^2 .

The measurement vectors used for updating the estimate are

$$\mathbf{z}_L^{\text{KF}} = [{}^L\mathbf{d}]_{3 \times 1}, \quad \mathbf{z}_V^{\text{KF}} = [z_x^{\text{T}} \quad z_v^{\text{T}} \quad z_\phi \quad z_\omega]_{8 \times 1}^{\text{T}}, \quad (13)$$

where \mathbf{z}_L^{KF} is constructed each time a new LiDAR detection ${}^L\mathbf{d}$ is associated to the estimate \mathbf{x}^{KF} . If the latest VIO pose from time t_l is newer than the latest LiDAR measurement from time t_k , the measurement vector \mathbf{z}_V^{KF} is used, with the position measurement calculated as

$$\mathbf{z}_{x[t_l]} = {}^L\mathbf{d}_{[t_k]} + {}^L\mathbf{R}(\theta) \left({}^V\mathbf{p}_{[t_l]} - {}^V\mathbf{p}_{[t_k]} \right), \quad (14)$$

where ${}^L\mathbf{d}_{[t_k]}$ is the latest LiDAR detection, ${}^V\mathbf{p}_{[t_l]}$ is the new VIO pose, ${}^V\mathbf{p}_{[t_k]}$ is the VIO pose interpolated to time t_k , and ${}^L\mathbf{R}(\theta)$ is the rotation matrix constructed from the latest NLS optimization output. The velocity measurement is calculated as

$$\mathbf{z}_{v[t_l]} = {}^L\mathbf{R}(\theta) {}^V\mathbf{v}_{[t_l]}, \quad (15)$$

where ${}^V\mathbf{v}_{[t_l]}$ is the velocity obtained from the VIO. The heading and heading rate measurements are constructed as

$$\mathbf{z}_{\phi[t_l]} = {}^V\phi_{[t_l]} - \theta, \quad \mathbf{z}_{\omega[t_l]} = {}^V\omega_{[t_l]}, \quad (16)$$

where ${}^V\phi_{[t_l]}$ is the heading of the VIO pose, θ is the relative heading obtained from the NLS optimization, and ${}^V\omega_{[t_l]}$ is the heading rate from the VIO output. If the received VIO pose is older than the latest LiDAR measurement, only the heading and heading rate states are updated with the measurement vector constructed as

$$\mathbf{z}_\phi^{\text{KF}} = [z_\phi \quad z_\omega]_{2 \times 1}^{\text{T}}, \quad (17)$$

where its elements are calculated by (16).

Measurement covariance matrix \mathbf{R}_L^{KF} is constructed as

$$\mathbf{R}_L^{\text{KF}} = \begin{bmatrix} \mathbf{R}_x^{\text{KF}} & \mathbf{0} & 0 & 0 \\ \mathbf{0} & \mathbf{R}_v^{\text{KF}} & 0 & 0 \\ 0 & 0 & R_\phi^{\text{KF}} & 0 \\ 0 & 0 & 0 & R_\omega^{\text{KF}} \end{bmatrix}, \quad (18)$$

where the individual submatrices \mathbf{R}_a^{KF} are obtained by propagating the uncertainty of the individual measurements from equations (14), (15), and (16) as

$$\mathbf{R}_a^{\text{KF}} = \mathbf{J}_a \mathbf{R}_a^{\text{orig}} \mathbf{J}_a^{\text{T}}, \quad (19)$$

where \mathbf{J}_a is the Jacobian matrix of the respective measurement functions (14), (15), or (16), and $\mathbf{R}_a^{\text{orig}}$ is the covariance matrix of the original measurements. The measurement noise is assumed to be isotropic, thus the measurement covariance matrices depend on the detection variance σ_d^2 , relative heading variance σ_θ^2 , VIO relative vector variance σ_r^2 , VIO linear velocity variance σ_v^2 , VIO heading variance σ_ϕ^2 , and VIO heading rate variance σ_ω^2 .

New LiDAR detections are associated to the estimate \mathbf{x}^{KF} based on their Euclidean and Mahalanobis distance. If the Euclidean distance of a detection from the estimate is lower than a predefined threshold, its squared Mahalanobis distance from the estimate at the corresponding time is calculated as

$$\delta_{[t_k]}^2 = \mathbf{y}_{[t_k]}^{\text{T}} \mathbf{S}_{[t_k]}^{-1} \mathbf{y}_{[t_k]}, \quad (20)$$

where $\mathbf{y}_{[t_k]}$ is the measurement innovation and $\mathbf{S}_{[t_k]}$ is the innovation covariance calculated during the LKF correction. The detection with the lowest Mahalanobis distance $\delta_{[t_k]}$ is selected and associated to the estimate if it is lower than a predefined threshold.

3) Estimate initialization

The *LiDAR-based detector* provides a set of detections ${}^L D$ of all the tracked flying objects in the surrounding environment. The *UAV pose estimator* constructs a separate detection buffer for each tracked object and performs the NLS trajectory alignment (3) for each detection buffer and the VIO pose buffer. If the buffers contain sufficient movement of the UAV and the NLS optimization converges to a solution with the final cost below a specified threshold, the estimate is initialized based on this detection buffer.

4) Reference transformer

The *Reference transformer* utilizes the relative transformation ${}^S_L \mathbf{T}$ produced by the estimator to transform the desired trajectory ${}^L \mathcal{X}_{\text{in}}$ to the secondary UAV reference frame S . The reference transformer keeps track of what part of the desired trajectory has already been completed in order to transmit only unvisited parts and repeatedly transmits references to the secondary UAV at the rate of 5 Hz. On board the secondary UAV, the *Goal receiver* module receives the trajectories and checks them for time stamp inconsistencies before transferring them to the secondary UAV control pipeline.

C. ANALYSIS OF DEGENERATE CASES

In the proposed approach, these degenerate cases can arise:

1) Loss of LiDAR detections ${}^L d$

When line-of-sight visibility between the UAVs gets broken, the transformations ${}^S_L \mathbf{T}$ and ${}^V_L \mathbf{T}$ become unobservable. The

estimator will keep tracking the UAV from the VIO poses transformed using the latest ${}^V_L \mathbf{T}$ (see (13)-(16)), but the estimated UAV pose in the frame L will drift away from its true value, as ${}^V_L \mathbf{T}$ will not be getting updated. When visibility between the UAVs gets re-established, the estimate will be corrected or re-initialized.

2) Loss of VIO poses ${}^V p$

When communication between the UAVs gets broken, its 3D position ${}^L_S \mathbf{x}$ is still observable from the LiDAR data, but the transformation ${}^V_L \mathbf{T}$ and the heading ${}^L \phi$ of the secondary UAV become unobservable. The estimator will keep tracking the UAV but will not update the ${}^L \phi$ and ${}^L \omega$ states during the loss of communication.

3) Small translational motion of the secondary UAV

The relative transformation ${}^V_L \mathbf{T}$ becomes unobservable as the UAV trajectory in the sliding window degrades to a single point. If the observed UAV motion falls to the level of the LiDAR measurement noise, the resulting estimate will become inconsistent. Such a situation is detected based on the trajectory length in the window and the eigenvalues of the Fisher information matrix

$$\mathbf{F} \left(\begin{matrix} V \\ L \end{matrix} \hat{\mathbf{t}}, \hat{\theta} \right) = \mathbf{J} \left(\begin{matrix} V \\ L \end{matrix} \hat{\mathbf{t}}, \hat{\theta} \right)^{\text{T}} \mathbf{J} \left(\begin{matrix} V \\ L \end{matrix} \hat{\mathbf{t}}, \hat{\theta} \right), \quad (21)$$

constructed from the Jacobian \mathbf{J} evaluated when solving the NLS problem. As the optimization problem becomes degenerate, the lowest eigenvalue of the matrix \mathbf{F} tends to zero. If the eigenvalue falls below a predefined threshold, the estimator stops updating ${}^V_L \mathbf{T}$.

III. EXPERIMENTAL VERIFICATION

Video of the experimental verification is available online ².

A. SIMULATIONS

1) Drift compensation

Simulations in the Gazebo simulator were performed to evaluate the ability to compensate for the odometry drift. The simulations were performed in an indoor environment with no obstacles breaking the line of sight between the UAVs (see the multimedia attachment). In the simulated scenario, the primary UAV moved in a 3 by 3 m large square while guiding the secondary UAV to follow a surrounding circular trajectory with the radius of 4 m at the velocity of 0.5 m s^{-1} (see Fig. 5). The trajectories were predefined in the LiDAR SLAM reference frame. In each run of the simulation, the secondary UAV was tasked to complete the circle 10 times.

The primary UAV carried a simulated LiDAR with the same parameters as its real-world counterpart from Sec. III-B and utilized it in the LOAM [54] SLAM algorithm. Instead of real VIO, the secondary UAV control loop used ground-truth localization with artificially inserted constant-velocity drift in the x -axis. The approach was evaluated for drift values

²<http://mrs.felk.cvut.cz/coop-fusion>

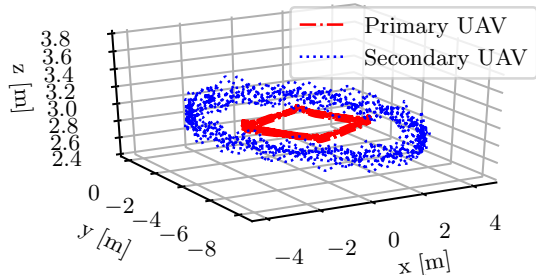


FIGURE 5. Trajectories in the simulation with zero drift.

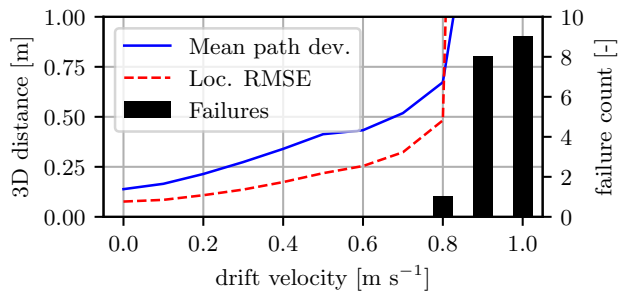


FIGURE 6. Mean deviation from the circular path, relative localization RMSE, and failure count for each drift value.

ranging from 0 to 1 m s^{-1} with the step of 0.1 m s^{-1} . For each drift value, the simulation was done 10 times. The simulation run was considered to be a failure, if the secondary UAV failed to complete the 10 circles, e.g., due to collision with the surrounding obstacles.

Fig. 6 shows the mean deviation from the circular path, the Root Mean Squared Error (RMSE) of the relative localization, and the number of runs in which the UAV failed to complete the 10 circles. The simulations were completely successful for drift values up to 0.7 m s^{-1} and with one failure for the drift of 0.8 m s^{-1} . The mean path deviation ranged from 0.14 m in the case of zero drift up to 0.67 m in the case of 0.8 m s^{-1} drift. The relative localization RMSE ranged from 0.08 m up to 0.48 m.

2) Non-Line-of-Sight (NLOS) simulation

The approach was evaluated in a simulated NLOS situation. The primary UAV moved back and forth in a line and guided the secondary UAV to follow a trajectory passing through a 1 m wide gap and behind a wall (see Fig. 8). The secondary UAV was $0.45 \text{ m} \times 0.45 \text{ m}$ wide including propellers. The secondary UAV performed the loop 10 times. Two additional UAVs hovered next to the desired trajectory to demonstrate the robustness of the approach to false detections. As in the previous simulation, the primary UAV carried a simulated Ouster OS0-128 3D LiDAR with the LiDAR data utilized by the LOAM [54] SLAM. The secondary UAV carried a fisheye camera with IMU corresponding to those used in the real-world experiments and utilized VINS-Mono [55] in its control loop.

Fig. 9 shows the progression of the localization error of the

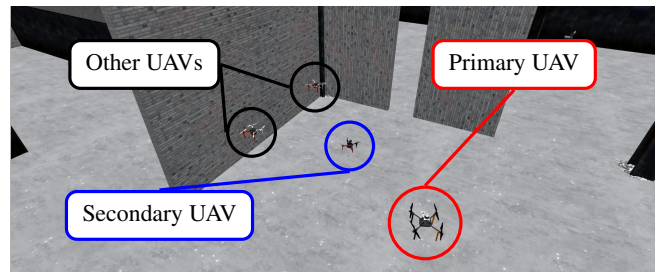


FIGURE 7. NLOS experiment in the Gazebo simulator.

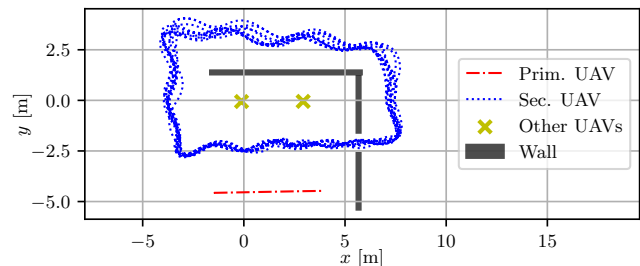


FIGURE 8. Ground-truth trajectories from NLOS simulation.

proposed fusion approach with respect to the ground truth. When the visibility was lost, the localization started drifting but was corrected each time when the visibility was re-established. The position RMSE was 0.11 m when the UAV was tracked by the primary UAV (calculated from the localization data obtained at the time periods when the secondary UAV was detected in the LiDAR data) and 0.35 m when it was out of sight.

B. REAL-WORLD LOCALIZATION AND GUIDANCE EVALUATION

To the best of the authors' knowledge, there are not yet any standard datasets containing multiple UAVs with LiDAR data and heterogeneous localization methods, usable for testing such an approach, as proposed in this paper. Therefore, the raw data from the real-world flights performed in this work have been released online³ to enable reproducibility of our results and provide data useful for developing such relative localization approaches to the research community. As there are no existing, openly-available algorithms utilizing the same hardware setup and alternative relative localization approaches require fundamentally different hardware on either one or both UAVs, making direct experimental comparison infeasible, the following quantitative evaluation of the proposed approach focuses mainly on the localization improvements provided by the fusion method with respect to the VIO-only output.

1) Experimental setup

The UAV platforms are shown in Fig. 10. For a detailed description of the UAV hardware, see [56]. The primary UAV

³https://github.com/ctu-mrs/coop_uav_dataset

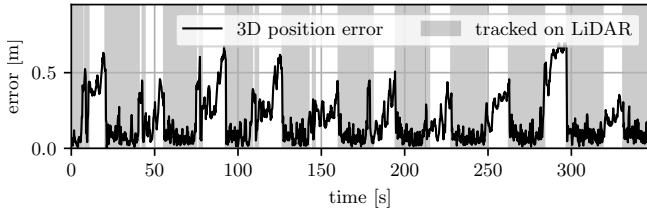


FIGURE 9. Relative localization error from NLOS simulation.

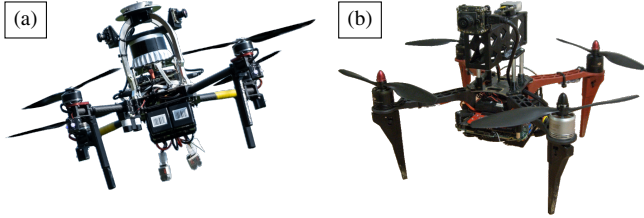


FIGURE 10. UAV platforms employed in the real-world experiments: (a) primary UAV carrying the Ouster 3D LiDAR, (b) secondary UAV with the monocular camera.

is built upon the X500 frame and carries the Intel NUC 10i7FNH onboard computer with the Intel Core i7 10710U CPU, 16 GB of RAM, and a Wi-Fi module. The secondary UAV is built upon the F330 frame and carries the Intel NUC 8i7BEH with the Intel Core i7-8559U CPU and 16 GB RAM. Both UAVs carry the Pixhawk 4 FCU containing the embedded attitude controller.

The primary UAV carries the Ouster OS0-128 Rev C 3D LiDAR. The LiDAR weighs 430 g without its top radial cap, has a 360° horizontal and 90° vertical FOV, and produces scans with the resolution of 1024×128 beams at a rate of 10 Hz. The primary UAV utilizes the LOAM SLAM algorithm [54] for its self-localization.

The secondary UAV carries the front-facing Bluefox MLC200Wc camera with the DSL217 fisheye lens. The camera is rigidly connected to the ICM-42688-P IMU. The camera produces images at the rate of 30 Hz at 752×480 resolution. For self-localization, the secondary UAV utilizes the VINS-Mono algorithm [55] with disabled loop closure detection. The VINS-Mono algorithm processes the images at the rate of 10 Hz and the IMU at the rate of 1000 Hz. The UAV is equipped with the Emlid Reach Real-time kinematic (RTK) module for ground truth recording.

The software on board the UAVs is based on Ubuntu 20.04, Robot Operating System (ROS) 1, and the MRS UAV system [50]. Nimbro network is used for transporting the ROS topics over the wireless network. The system time of the onboard computers of the UAVs is synchronized using chrony⁴ with the primary UAV acting as a server and the secondary UAV acting as a client. All algorithms ran entirely on board the UAVs. The RTK data were collected for offline ground truth comparison and were not utilized in the control loop of the UAVs in any way.

The ground truth comparison was performed based on the

⁴<https://chrony.tuxfamily.org>

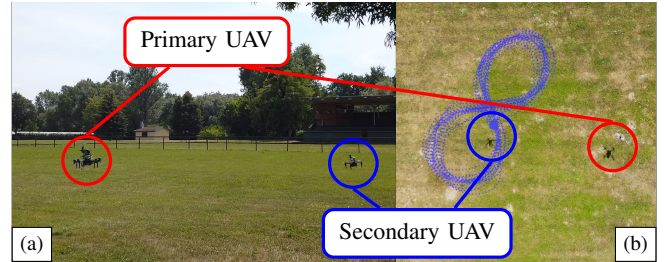


FIGURE 11. Side view (a) and top-down view (b) of the experimental verification. Ground-truth trajectory of the secondary UAV is drawn over the image.

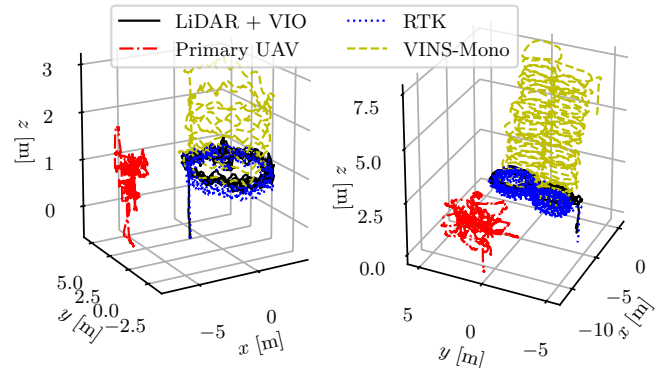


FIGURE 12. Trajectories from the real-world flights.

trajectory evaluation methods described in [57]. Each evaluated trajectory was aligned with the RTK ground truth data based on the first 20 seconds of each data series. The error at each data point was calculated as the Euclidean distance between the aligned trajectory and the ground truth. For each trajectory, the 2D and 3D Absolute Trajectory Errors (ATEs) were calculated as the total RMSE between the ground truth and the aligned trajectory.

2) Results

The secondary UAV trajectory was predefined in the LiDAR SLAM frame, and the primary UAV guided the secondary UAV to follow the trajectory based on its commands. Two trajectories were evaluated: a circle with 0.5 m s^{-1} velocity and a figure eight with 1 m s^{-1} velocity. The UAV faced the direction of its movement. The primary UAV was commanded by an operator to keep changing its pose while being stabilized based on its LiDAR localization. In the circular flight, the mutual UAV distance ranged between 3.2 m to 10.9 m with a mean of 7.0 m. In the figure-eight flight, the distance ranged between 2.5 m to 9.8 m with a mean of 6.3 m. The algorithms proved capable of real-time usage on board the UAVs with the LiDAR-based detector producing detections at the rate of 10 Hz and the fusion algorithm taking less than 5 ms to fuse them to produce each estimate.

The data from flights, aligned to a common reference frame, are shown in Fig. 12. In both cases, the VIO output exhibited significant drift, mainly in the direction of the

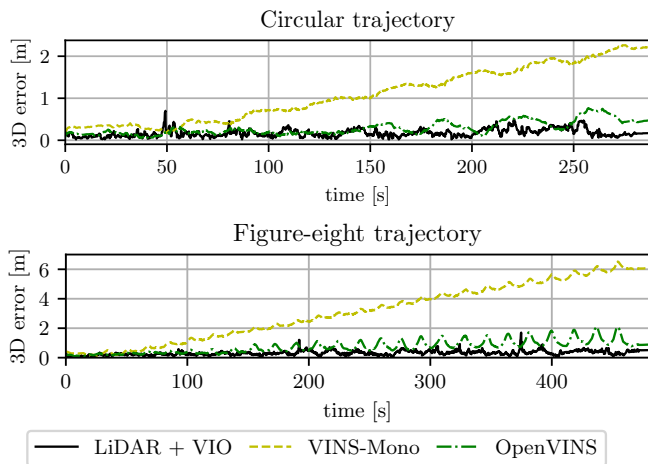


FIGURE 13. Progression of 3D localization error over time from both of the performed trajectories. The error was calculated as the Euclidean distance between the RTK ground truth and the respective aligned trajectory.

z -axis. Despite the drift, the proposed method accurately tracked the secondary UAV and enabled correct guidance of the UAV along the desired trajectories. Fig. 13 compares the localization error of the LiDAR + VIO fusion, VINS-Mono, and OpenVINS. OpenVINS [58] was run offline using the collected data for error comparison. While the output of the VIO methods was constantly drifting, the error of the LiDAR + VIO fusion was unaffected by this drift. The data shows that drift between two VIO methods can significantly differ, even if they use the same data, making the drift values difficult to estimate beforehand. Furthermore, the amount of drift can change with texture in the scene, illumination, propeller-induced vibrations picked up by the IMU, etc.

Table 1 contains the ATEs of the LiDAR + VIO fusion and the tested VIO methods. Both the 3D error and the 2D error in the xy -plane are provided, as the VINS-Mono drift was most significant in the z -axis, and the LiDAR vertical resolution is lower than its horizontal resolution. The 3D ATE of the LiDAR + VIO fusion was 0.19 m in the circular flight and 0.36 m in the figure-eight flight, significantly lower than the errors of the VIO output. The fusion error in the figure-eight flight was larger than that of the circular flight due to the greater velocity of the secondary UAV. The experimental evaluation showed that guidance based on the LiDAR + VIO fusion is capable of mitigating the effects of the VIO drift on the flight of the secondary UAV.

TABLE 1. Overall ATEs in meters, calculated as the RMSE of all aligned data points.

Trajectory	LiDAR + VIO		VINS-Mono		OpenVINS	
	2D	3D	2D	3D	2D	3D
circle	0.13	0.19	0.49	1.21	0.28	0.32
eight	0.22	0.36	1.44	3.55	0.68	0.83
Average	0.18	0.28	0.97	2.38	0.48	0.58



FIGURE 14. The UAVs mapping an industrial warehouse.

C. REAL-WORLD COOPERATIVE MAPPING SCENARIO

The proposed relative localization method was applied to a cooperative mapping scenario to enable occupancy mapping of an industrial warehouse using a heterogeneous UAV team (see Fig. 14 and the multimedia attachment⁵).

The experiment demonstrated that the proposed method is sufficiently accurate to enable precise cooperative mapping of a complex real-world environment. The deployed UAVs were identical to the platforms described in Sec. III-B1, except that the secondary UAV was equipped with RealSense T265 tracking camera for VIO and RealSense D435 depth camera for dense occupancy mapping. The secondary UAV utilized OpenVINS [58] as the VIO algorithm. The secondary UAV was equipped with reflective markers on its legs to provide an additional safety feature for robust performance of the LiDAR-based detection algorithm in the cluttered environment. The size of the reflective markers was designed taking into account the parameters of the Ouster OS0-128 LiDAR, such that the markers would be larger than the spread between the adjacent LiDAR beams up to the distance of 8 m. Both UAVs carried the Intel NUC 10i7FNH onboard computer.

In the experiment, the primary UAV stayed in a wide main corridor, while the secondary UAV was sent to map narrow side corridors. Desired goals for both UAVs were selected by the operator during the experiment based on the online-generated map. The primary UAV flew to selected goal points and guided the secondary UAV for brief periods before the secondary UAV flew into the side corridors. After the secondary UAV flew into each side corridor, it performed autonomous exploration of the area for a predefined amount of time. While exploring the side corridors, the secondary UAV was not tracked on LiDAR for part of its flight due to occlusions (see Fig. 15), therefore its estimated pose was updated only based on the incoming VIO data.

Each UAV constructed a local occupancy map online from its onboard sensors. The secondary UAV transmitted its local map to the primary UAV over the wireless network at the rate of 0.5 Hz. The local maps were merged together onboard the primary UAV using the output of the proposed relative local-

⁵<https://mrs.fel.cvut.cz/coop-fusion>

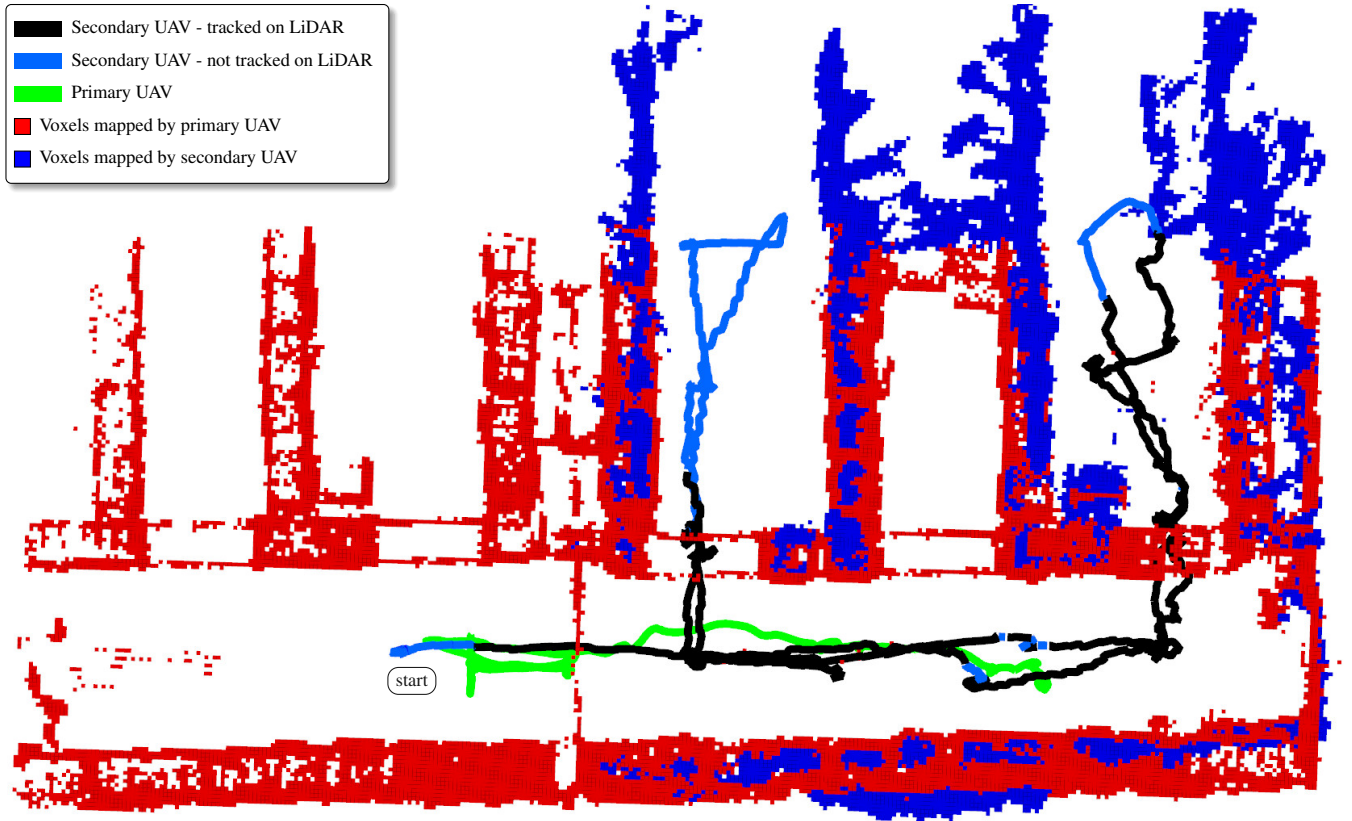


FIGURE 15. UAV trajectories and projection of the global occupancy map obtained during the real-world cooperative mapping experiment in an industrial warehouse.

ization method. The obtained global occupancy map is shown in Fig. 15. The results of the experiment qualitatively evaluate the accuracy of the proposed method and showcase that it can run on board the UAVs as a part of a complex software stack aimed for, e.g., autonomous cooperative exploration and mapping.

D. TUNING METHODOLOGY, PARAMETER SENSITIVITY, AND MEASUREMENT DELAY INFLUENCE ANALYSIS

To tune the parameters of the proposed method and evaluate its robustness, a simulation was designed in the Gazebo robotic simulator. The secondary UAV was following a figure-eight trajectory, while the primary UAV was following a line trajectory next to it (see Fig. 16). The LOAM algorithm was run on the LiDAR data of the primary UAV and the OpenVINS algorithm was run on the monocular camera data of the secondary UAV for localization. While the LiDAR-based localization was reliable throughout the flight, the VIO exhibited significant drift. Data recorded in this simulation were used to tune the algorithm and perform the parameter sensitivity and measurement delay influence analyses.

1) NLS-based estimator

Fig. 17 shows the dependency of the relative transformation $V_L T$ RMSE on the length of the sliding window in the NLS-based estimator. The RMSE was measured for 26 length

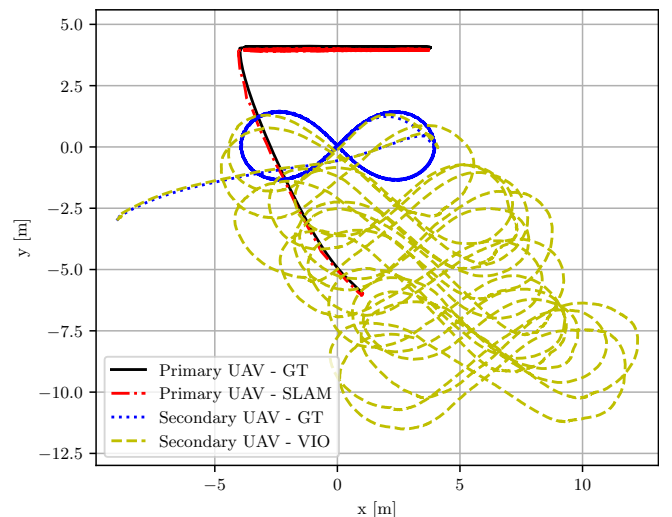


FIGURE 16. Ground-truth and estimated trajectories from the tuning and parameter sensitivity analysis.

values ranging from 2 to 330 s. For short sliding windows, the RMSE was large as the estimate was corrupted by measurement noise. The RMSE reached the lowest values for 25 s in the case of the translational error and 50 s in the case of the rotational error. For longer sliding windows, the RMSE gradually increased due to increasing lag of the estimate.

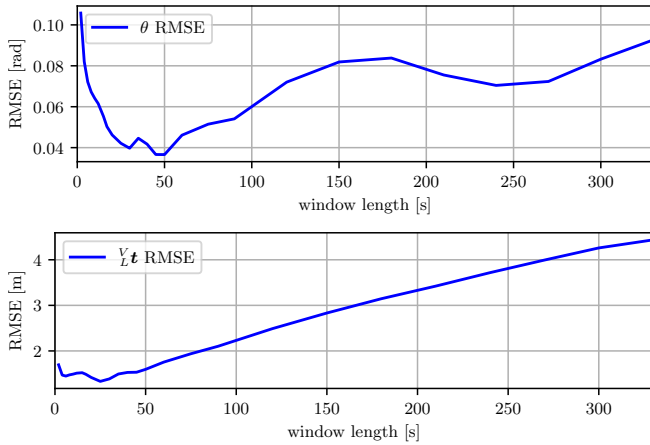


FIGURE 17. Dependency of the relative transformation $V_L T$ RMSE on the sliding-window length.

Based on the results, setting the sliding window length to a value in the range between 20 s and 50 s is advisable to obtain reliable estimator performance.

2) LKF-based tracker

The LKF-based tracker was tuned by analysing the performance of the algorithm with respect to the ground truth data in the simulated scenario. The measurement noise parameters, namely the detection variance σ_d^2 , relative heading variance σ_θ^2 , VIO relative vector variance σ_r^2 , VIO linear velocity variance σ_v^2 , VIO heading variance σ_ϕ^2 , and VIO heading rate variance σ_ω^2 , were measured in the simulation and set accordingly. The process noise parameters include the linear velocity variance σ_v^2 and the angular velocity variance σ_ω^2 . The process noise parameters were tuned by analysing the Average Normalized Estimation Error Squared (ANEES) [59] of the final estimate with respect to the ground-truth data and tuning the parameters to achieve consistent estimation performance, i.e., so that the ANEES over the dataset corresponds to the degrees of freedom of the state vector.

To tune the parameter σ_v^2 and to determine the effect of the parameter setting on the tracker output, UAV pose estimator was run on the simulation dataset for a set of 30 logarithmically-spaced values of σ_v^2 ranging from 0.01 to $100 \text{ m}^2\text{s}^{-2}$. Fig. 18 shows the dependency of the positional RMSE and of the ANEES of 3D position and linear velocity on different values of σ_v^2 . The best performance was obtained for σ_v^2 close to $0.1 \text{ m}^2\text{s}^{-2}$. For lower values of σ_v^2 , the tracker exhibits increasing lag of the estimate, with too large lag resulting in loss of tracking as the distance of the incoming detections from the estimate becomes larger than the association threshold. For larger values of σ_v^2 , the resulting estimate is underconfident and the measurement noise is not filtered properly. Fig. 19 shows the dependency of the heading RMSE and ANEES on the values of σ_ω^2 , ranging between 10^{-5} and $10^3 \text{ rad}^2\text{s}^{-2}$. The best ANEES was achieved for the value of $0.05 \text{ rad}^2\text{s}^{-2}$. The heading measurements in the simulation were not subject to significant Gaussian noise, therefore the

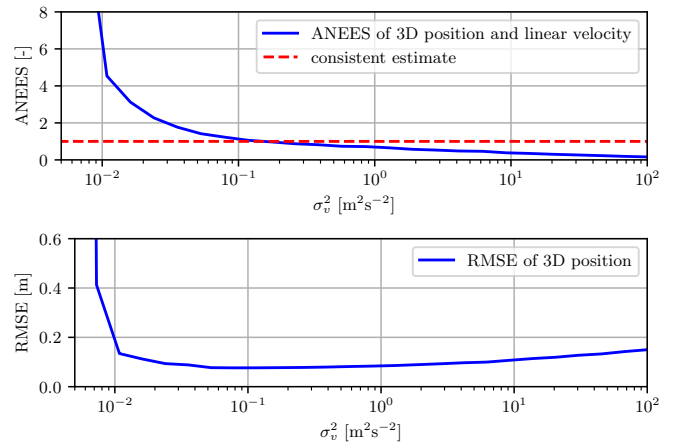


FIGURE 18. Dependencies of the positional RMSE and of the ANEES of 3D position and linear velocity on σ_v^2 . The ANEES was normalized by the number of DOFs. ANEES of one corresponds to a consistent estimate.

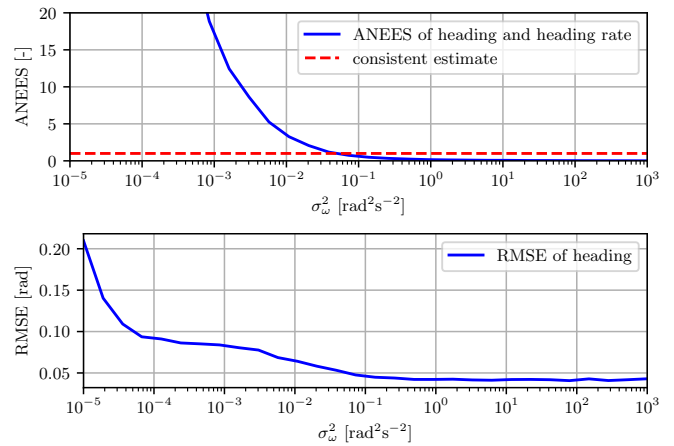


FIGURE 19. Dependencies of the heading RMSE and of the ANEES of the heading and heading rate on σ_ω^2 . The ANEES was normalized by the number of DOFs. ANEES of one corresponds to a consistent estimate.

RMSE exhibited low values even for higher values of σ_ω^2 .

3) Measurement delay influence analysis

Fig. 20 analyzes the dependency of localization error on the delay of the incoming VIO measurements. The simulation was performed for 41 communication-delay values ranging from 0 to 2 s. The positional accuracy of the proposed method depends mainly on the accuracy of the LiDAR detections with the VIO measurements improving the performance when the LiDAR detections are unavailable. For the VIO delay values from 0 to 0.5 s, the positional RMSE was slowly rising as the amount of VIO measurements usable in the case of LiDAR detection dropouts or large detection delay was decreasing. In the simulations, there were no significant LiDAR detection dropouts longer than 0.5 s, therefore the positional RMSE remained approximately constant for larger VIO delay values. The heading of the UAV is observed solely from the VIO measurements. Therefore, the heading accuracy kept growing with the increasing VIO delay.

Fig. 21 shows the dependency of the localization error

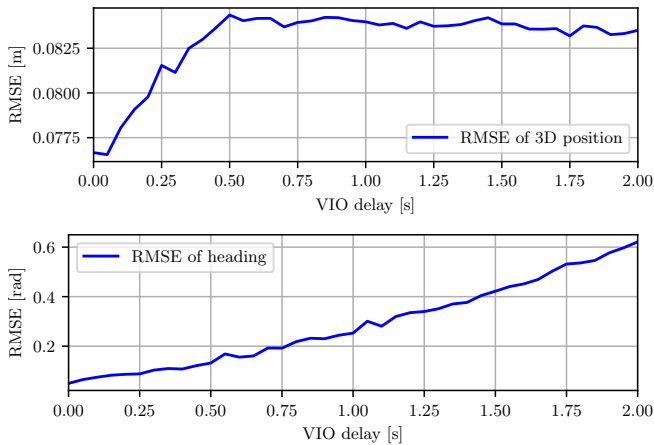


FIGURE 20. Dependency of positional and heading RMSE on the delay of the incoming VIO measurements.

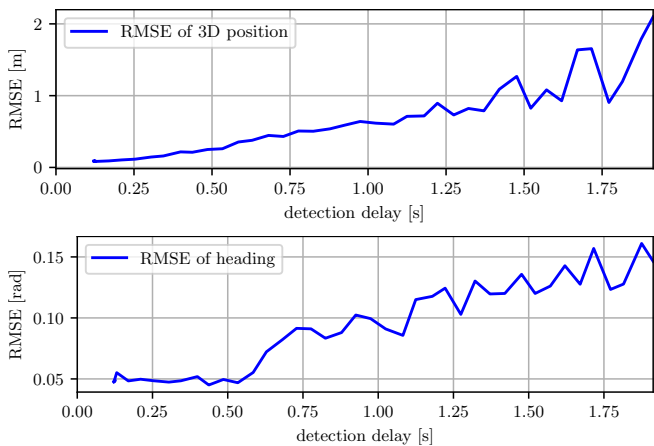


FIGURE 21. Dependency of positional and heading RMSE on the delay of the LiDAR detections.

on the average delay of the LiDAR detections. The LiDAR detection delay influences mainly the positional error, which grew linearly from 0.09 m for the average delay of 0.12 s to 2.10 m for the average delay of 1.91 s. The heading error slightly increased with growing detection delay due to the growing inaccuracy in the estimated relative transformation ${}^V_L\mathbf{T}$.

E. DISCUSSION

1) Scaling to more secondary UAVs

This work focused on the fundamental design of the fusion and guidance method for a single primary and secondary UAV pair and an exhaustive experimental study on scaling the approach to larger swarms is reserved for future work. Nevertheless, we shall discuss two important aspects for scaling the approach to multiple UAVs: the communication requirements and the initialization of the approach. Table 2 shows the communication requirements recorded in the real-world experiments in Sec. III-B and Sec. III-C. The communication from the secondary UAV to the primary UAV is constant, and the bandwidth is proportional to the rate of transmitted

messages. In the experiments, the bandwidth for a single UAV was 1.45 KB/s. The communication from the primary UAV to the secondary UAV depends on the rate of communication and on the number of points in the transmitted trajectory messages. In the implementation, each trajectory point was represented by 32 bytes. In the experiments, the bandwidth ranged from 0.61 KB/s to 30.53 KB/s. The communication requirements will scale linearly with the number of secondary UAVs, since all the secondary UAVs will need to receive and transmit data to the primary UAV, but the secondary UAVs will not communicate among themselves, and will scale linearly with the number of points in the reference trajectory. The TP-Link TL-WR902AC WiFi router was utilized in the experiments. The router has a maximum data transfer rate of 433 Mb/s over a 5 GHz network. Assuming the maximum bandwidth required by the approach to be 32 KB/s and no other data transmission required, the router is theoretically capable of supporting up to 1691 such transmissions. As such, the communication requirements are well below the capabilities of current wireless communication modules and will not restrict scaling of the approach to multiple secondary UAVs.

For initialization of the approach, the proposed approach requires that each secondary UAV performs a separate initialization maneuver to initialize the method as described in Sec. II-B3. The number of required initialization maneuvers scales linearly with the number of secondary UAVs.

As shown in [30], the employed UAV detection approach is capable of detecting multiple targets simultaneously and does not impede scaling the approach to multiple secondary UAVs.

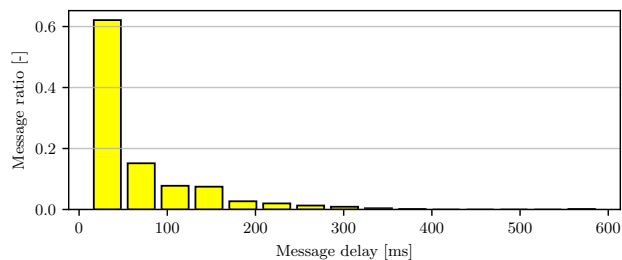
2) Operational limits of the system

As shown in Sec. III-A1, for the tested configuration the guidance of the secondary UAV based on the LiDAR detections was able to compensate for constant-velocity odometry drift of the secondary UAV for drift velocities of up to 0.7 m/s and with one failure for the value of 0.8 m/s. In case of a complete and sudden divergence of the VIO estimate, resulting in larger drift, the proposed method would not be able to compensate for it. The proposed approach is designed for drift compensation rather than failure recovery. Consequently, handling a catastrophic VIO failure, e.g., a total loss of tracking, is considered outside the current scope of this work. The method also fully relies on the yaw estimate from the VIO, as the LiDAR detections do not provide any information about the orientation of the secondary UAV. Therefore, in case of a complete failure of the VIO, the fusion method would not be able to obtain the yaw orientation of the secondary UAV. As this paper focuses on the fundamental estimation framework, a fallback solution for providing the secondary UAV's yaw is outside the scope of this work. In a practical application in a production-ready system, such a problem might be solved, e.g., by fusion of magnetometer data.

The maximum range of the method depends on the maximum range of the LiDAR sensor. In case of the utilized Ouster OS0-128 Rev C, the maximum range was 45 meters

TABLE 2. Analysis of the wireless communication requirements during the real-world experiments.

	Rate [Hz]	Message size [KB] (min/max)	Bandwidth [KB/s] (min/max)
Sec.→Prim. (odometry)	2	0.725 / 0.725	1.45 / 1.45
Prim.→Sec. - Exp. III-B	5	0.121 / 6.105	0.61 / 30.53
Prim.→Sec. - Exp. III-C	5	0.132 / 2.457	0.66 / 12.29

**FIGURE 22.** Histogram of VIO message delays from the cooperative mapping experiment.

at 80% Lambertian reflectivity with >90% detection probability⁶. Also, with increasing distances, the secondary UAV may not be detected if it is smaller than the spread between two adjacent LiDAR beams and falls between that spread. Such details regarding the LiDAR-based UAV detection are described in [30].

Large communication latency can be compensated for by the recalculating history buffer [52] used by the approach. Delayed measurements will be fused correctly, assuming that they are not older than the size of the history buffer. To showcase the real-world communication delays the system faced in the experiments, Fig. 22 shows the VIO message delays from the real-world deployment in the cooperative mapping scenario described in Sec. III-C. The VIO message delay ranged from 13 ms to 589 ms with the median delay of 39 ms. To account for packet loss, the estimator utilizes the constant-velocity model, which predicts the state of the secondary UAV if no measurements are received.

Under poor visibility, the method would benefit from the robustness of the LiDAR sensor, which can work even in darkness. However, the method would be unable to compensate for total VIO failure, as explained above. In case of occlusions and NLOS situations, the method will keep estimating the pose of the secondary UAV based on the incoming VIO data, as demonstrated in Sec. III-A2. When the line-of-sight gets re-established, new detections will be associated to the estimate, and VIO drift will be corrected. In case of too large VIO drift during the NLOS situation, the estimate will be re-initialized after a sufficient amount of detections is obtained. The re-initialization is retried periodically while the estimator is receiving VIO data over the wireless network.

⁶<https://data.ouster.io/downloads/datasheets/datasheet-revc-v2p5-os0.pdf>, accessed 23/07/2025

IV. CONCLUSIONS

An approach for cooperative guidance of a micro-scale UAV relying on a novel technique of relative localization was proposed in this paper. We proposed a heterogeneous UAV team consisting of a LiDAR-equipped primary UAV and a small camera-equipped secondary UAV, combining the benefits of both sensor types. To achieve the desired tight cooperation of UAVs with different sensory modalities, we proposed a novel approach for fusing the LiDAR relative localization with VIO output on board the primary UAV to obtain accurate pose of the secondary UAV. We demonstrated that the resulting pose estimate can be used to guide the secondary UAV along desired trajectories defined in the reference frame of the primary UAV. The performance of the proposed approach was verified and quantitatively evaluated in simulations and real-world experiments. The results showed the superior accuracy of the fusion output to the pure VIO data, successfully demonstrated the capability to guide the secondary UAV along the desired trajectories, and showcased the usability of the proposed approach in a cooperative mapping scenario.

REFERENCES

- [1] M. Petrlik, P. Petracek, V. Kratky, T. Musil, Y. Stasinchuk, M. Vrba, T. Baca, D. Hert, M. Pecka, T. Svoboda, and M. Saska, "UAVs Beneath the Surface: Cooperative Autonomy for Subterranean Search and Rescue in DARPA SubT," *Field Robotics*, vol. 3, pp. 1–68, January 2023.
- [2] V. Krátký, P. Petráček, T. Báča, and M. Saska, "An autonomous unmanned aerial vehicle system for fast exploration of large complex indoor environments," *Journal of Field Robotics*, vol. 38, no. 8, pp. 1036–1058, 2021.
- [3] J. Bednar, M. Petrlik, K. C. Teixeira Vivaldini, and M. Saska, "Deployment of Reliable Visual Inertial Odometry Approaches for Unmanned Aerial Vehicles in Real-world Environment," in *International Conference on Unmanned Aircraft Systems (ICUAS)*. IEEE, June 2022.
- [4] H. Lim, Y. Kim, K. Jung, S. Hu, and H. Myung, "Avoiding Degeneracy for Monocular Visual SLAM with Point and Line Features," in *IEEE International Conference on Robotics and Automation (ICRA)*, May 2021.
- [5] J. A. Hesch, D. G. Kottas, S. L. Bowman, and S. I. Roumeliotis, "Consistency Analysis and Improvement of Vision-aided Inertial Navigation," *IEEE Transactions on Robotics*, vol. 30, no. 1, pp. 158–176, Feb. 2014.
- [6] K. J. Wu and S. I. Roumeliotis, "Unobservable Directions of VINS Under Special Motions," Dept. of Computer Science and Engineering, University of Minnesota, Tech. Rep., 2016.
- [7] Y. Yang and G. Huang, "Observability Analysis of Aided INS With Heterogeneous Features of Points, Lines, and Planes," *IEEE Transactions on Robotics*, vol. 35, no. 6, pp. 1399–1418, Dec. 2019.
- [8] A. Geiger, P. Lenz, and R. Urtasun, "Are we ready for Autonomous Driving? The KITTI Vision Benchmark Suite," in *IEEE Conference on Computer Vision and Pattern Recognition (CVPR)*, 2012. [Online]. Available: http://www.cvlibs.net/datasets/kitti/eval_odometry.php
- [9] K. Ebadi, L. Bernreiter, H. Biggie, G. Catt, Y. Chang, A. Chatterjee, C. E. Denniston, S.-P. Deschênes, K. Harlow, S. Khattak, L. Nogueira, M. Palieri, P. Petráček, M. Petrlik, A. Reinke, V. Krátký, S. Zhao, A.-a. Agha-mohammadi, K. Alexis, C. Heckman, K. Khosoussi, N. Kottege, B. Morrell, M. Hutter, F. Pauling, F. Pomerleau, M. Saska, S. Scherer, R. Siegwart, J. L. Williams, and L. Carlone, "Present and Future of SLAM in Extreme Environments: The DARPA SubT Challenge," *IEEE Transactions on Robotics*, vol. 40, pp. 936–959, 2024.
- [10] V. Walter, N. Staub, A. Franchi, and M. Saska, "UVDAR System for Visual Relative Localization With Application to Leader-Follower Formations of Multirotor UAVs," *IEEE Robotics and Automation Letters*, vol. 4, no. 3, pp. 2637–2644, Jul. 2019.
- [11] F. Schilling, F. Schiano, and D. Floreano, "Vision-Based Drone Flocking in Outdoor Environments," *IEEE Robotics and Automation Letters*, vol. 6, no. 2, pp. 2954–2961, Apr. 2021.
- [12] M. Vrba and M. Saska, "Marker-Less Micro Aerial Vehicle Detection and Localization Using Convolutional Neural Networks," *IEEE Robotics and Automation Letters*, vol. 5, no. 2, pp. 2459–2466, Apr. 2020.

- [13] R. Ge, M. Lee, V. Radhakrishnan, Y. Zhou, G. Li, and G. Loianno, "Vision-based Relative Detection and Tracking for Teams of Micro Aerial Vehicles," in *IEEE/RSJ International Conference on Intelligent Robots and Systems (IROS)*, Oct. 2022.
- [14] M. Pavliv, F. Schiano, C. Reardon, D. Floreano, and G. Loianno, "Tracking and Relative Localization of Drone Swarms With a Vision-Based Headset," *IEEE Robotics and Automation Letters*, vol. 6, no. 2, pp. 1455–1462, Apr. 2021.
- [15] M. Křifžek, M. Vrba, A. B. Kulaš, S. Bogdan, and M. Saska, "Bio-inspired visual relative localization for large swarms of UAVs," in *2024 IEEE International Conference on Robotics and Automation (ICRA)*, May 2024.
- [16] Y. Zhang, Z. Ning, X. Zhang, S. Guo, P. Liu, and S. Zhao, "EvDet-MAV: Generalized MAV Detection From Moving Event Cameras," *IEEE Robotics and Automation Letters*, vol. 10, no. 8, pp. 8236–8243, Aug. 2025.
- [17] H. Guo, C. Zheng, and S. Zhao, "Motion-guided small MAV detection in complex and non-planar scenes," *Pattern Recognition Letters*, vol. 186, pp. 98–105, Oct. 2024.
- [18] Y. Zheng, C. Zheng, J. Shen, P. Liu, and S. Zhao, "Keypoint-Guided Efficient Pose Estimation and Domain Adaptation for Micro Aerial Vehicles," *IEEE Transactions on Robotics*, vol. 40, pp. 2967–2983, 2024.
- [19] L. Guo, Z. Gongye, Z. Xu, Y. Wang, X. Zhou, J. Zhou, and F. Gao, "Preserving Relative Localization of FoV-Limited Drone Swarm via Active Mutual Observation," in *2024 IEEE/RSJ International Conference on Intelligent Robots and Systems (IROS)*, Oct. 2024.
- [20] K. Guo, X. Li, and L. Xie, "Ultra-Wideband and Odometry-Based Cooperative Relative Localization With Application to Multi-UAV Formation Control," *IEEE Transactions on Cybernetics*, vol. 50, no. 6, pp. 2590–2603, Jun. 2020.
- [21] Y. Huang, T. Shan, F. Chen, and B. Englot, "DiSCo-SLAM: Distributed Scan Context-Enabled Multi-Robot LiDAR SLAM With Two-Stage Global-Local Graph Optimization," *IEEE Robotics and Automation Letters*, vol. 7, no. 2, pp. 1150–1157, Apr. 2022.
- [22] Y. Chang, K. Ebadi, C. E. Denniston, M. F. Ginting, A. Rosinol, A. Reinke, M. Palieri, J. Shi, A. Chatterjee, B. Morrell, A.-a. Agha-mohammadi, and L. Carlone, "LAMP 2.0: A Robust Multi-Robot SLAM System for Operation in Challenging Large-Scale Underground Environments," *IEEE Robotics and Automation Letters*, vol. 7, no. 4, pp. 9175–9182, Oct. 2022.
- [23] Y. Tian, Y. Chang, F. H. Arias, C. Nieto-Granda, J. P. How, and L. Carlone, "Kimera-Multi: Robust, Distributed, Dense Metric-Semantic SLAM for Multi-Robot Systems," *IEEE Transactions on Robotics*, pp. 1–17, 2022.
- [24] Y. Jang, C. Oh, Y. Lee, and H. J. Kim, "Multirobot Collaborative Monocular SLAM Utilizing Rendezvous," *IEEE Transactions on Robotics*, vol. 37, no. 5, pp. 1469–1486, Oct. 2021.
- [25] R. Dubois, A. Eudes, and V. Frémont, "Sharing visual-inertial data for collaborative decentralized simultaneous localization and mapping," *Robotics and Autonomous Systems*, vol. 148, p. 103933, Feb. 2022.
- [26] J. Gross, M. De Petrillo, J. Beard, H. Nichols, T. Swiger, R. Watson, C. Kirk, C. Kilic, J. Hikes, E. Upton, D. Ross, M. Russell, Y. Gu, and C. Griffin, "Field-Testing of a UAV-UGV Team for GNSS-Denied Navigation in Subterranean Environments," in *Proceedings of the 32nd International Technical Meeting of the Satellite Division of The Institute of Navigation (ION GNSS+)*, Oct. 2019, pp. 2112–2124.
- [27] F. Zhu, Y. Ren, F. Kong, H. Wu, S. Liang, N. Chen, W. Xu, and F. Zhang, "Swarm-LIO: Decentralized Swarm LiDAR-inertial Odometry," in *IEEE International Conference on Robotics and Automation (ICRA)*, May 2023, pp. 3254–3260.
- [28] F. Zhu, Y. Ren, L. Yin, F. Kong, Q. Liu, R. Xue, W. Liu, Y. Cai, G. Lu, H. Li, and F. Zhang, "Swarm-LIO2: Decentralized Efficient LiDAR-Inertial Odometry for Aerial Swarm Systems," *IEEE Transactions on Robotics*, vol. 41, pp. 960–981, 2025.
- [29] M. Vrba, Y. Stasinchuk, T. Báča, V. Spurný, M. Petrlik, D. Heřt, D. Žaitlík, and M. Saska, "Autonomous capture of agile flying objects using UAVs: The MBZIRC 2020 challenge," *Robotics and Autonomous Systems*, vol. 149, p. 103970, Mar. 2022.
- [30] M. Vrba, V. Walter, V. Pritzl, M. Pliska, T. Báča, V. Spurný, D. Heřt, and M. Saska, "On Onboard LiDAR-Based Flying Object Detection," *IEEE Transactions on Robotics*, vol. 41, pp. 593–611, 2025.
- [31] F. Causa and G. Fasano, "Adaptive Cooperative Navigation Strategies for Complex Environments," in *IEEE/ION Position, Location and Navigation Symposium (PLANS)*, Apr. 2020, pp. 100–111.
- [32] F. Causa, R. Opromolla, and G. Fasano, "Cooperative navigation and visual tracking with passive ranging for UAV flight in GNSS-challenging environments," in *International Conference on Unmanned Aircraft Systems (ICUAS)*, Jun. 2021.
- [33] T.-M. Nguyen, M. Cao, S. Yuan, Y. Lyu, T. H. Nguyen, and L. Xie, "VIRAL-Fusion: A Visual-Inertial-Ranging-Lidar Sensor Fusion Approach," *IEEE Transactions on Robotics*, vol. 38, no. 2, pp. 958–977, Apr. 2022.
- [34] T. H. Nguyen, T.-M. Nguyen, and L. Xie, "Flexible and Resource-Efficient Multi-Robot Collaborative Visual-Inertial-Range Localization," *IEEE Robotics and Automation Letters*, vol. 7, no. 2, pp. 928–935, Apr. 2022.
- [35] T. Ziegler, M. Karrer, P. Schmuck, and M. Chli, "Distributed Formation Estimation Via Pairwise Distance Measurements," *IEEE Robotics and Automation Letters*, vol. 6, no. 2, pp. 3017–3024, Apr. 2021.
- [36] H. Xu, L. Wang, Y. Zhang, K. Qiu, and S. Shen, "Decentralized Visual-Inertial-UWB Fusion for Relative State Estimation of Aerial Swarm," in *IEEE International Conference on Robotics and Automation (ICRA)*, May 2020.
- [37] H. Xu, Y. Zhang, B. Zhou, L. Wang, X. Yao, G. Meng, and S. Shen, "Omni-Swarm: A Decentralized Omnidirectional Visual-Inertial-UWB State Estimation System for Aerial Swarms," *IEEE Transactions on Robotics*, pp. 1–21, 2022.
- [38] P. Zhang, G. Chen, Y. Li, and W. Dong, "Agile Formation Control of Drone Flocking Enhanced With Active Vision-Based Relative Localization," *IEEE Robotics and Automation Letters*, vol. 7, no. 3, pp. 6359–6366, Jul. 2022.
- [39] J. P. Queralta, Q. Li, F. Schiano, and T. Westerlund, "VIO-UWB-Based Collaborative Localization and Dense Scene Reconstruction within Heterogeneous Multi-Robot Systems," in *International Conference on Advanced Robotics and Mechatronics (ICARM)*, 2022.
- [40] I. Spasojevic, X. Liu, A. Ribeiro, G. J. Pappas, and V. Kumar, "Active Collaborative Localization in Heterogeneous Robot Teams," in *Robotics: Science and Systems*, vol. 19, Jul. 2023.
- [41] H. Yu, W. Zhen, W. Yang, J. Zhang, and S. Scherer, "Monocular Camera Localization in Prior LiDAR Maps with 2D-3D Line Correspondences," in *IEEE/RSJ International Conference on Intelligent Robots and Systems (IROS)*, Oct. 2020.
- [42] S. Cao, X. Lu, and S. Shen, "GVINS: Tightly Coupled GNSS-Visual-Inertial Fusion for Smooth and Consistent State Estimation," *IEEE Transactions on Robotics*, vol. 38, no. 4, pp. 2004–2021, Aug. 2022.
- [43] W. Lee, K. Eickenhoff, P. Geneva, and G. Huang, "Intermittent GPS-aided VIO: Online Initialization and Calibration," in *IEEE International Conference on Robotics and Automation (ICRA)*, May 2020.
- [44] K. Eickenhoff, Y. Yang, P. Geneva, and G. Huang, "Tightly-Coupled Visual-Inertial Localization and 3-D Rigid-Body Target Tracking," *IEEE Robotics and Automation Letters*, vol. 4, no. 2, pp. 1541–1548, Apr. 2019.
- [45] K. Eickenhoff, P. Geneva, N. Merrill, and G. Huang, "Schmidt-EKF-based Visual-Inertial Moving Object Tracking," in *IEEE International Conference on Robotics and Automation (ICRA)*, May 2020.
- [46] V. Pritzl, M. Vrba, P. Stepan, and M. Saska, "Cooperative Navigation and Guidance of a Micro-Scale Aerial Vehicle by an Accompanying UAV using 3D LiDAR Relative Localization," in *International Conference on Unmanned Aircraft Systems (ICUAS)*, IEEE, June 2022.
- [47] V. Pritzl, P. Štěpán, and M. Saska, "Cooperative flight in complex environments using heterogeneous uavs and lidar-based relative localization," in *Multi-Robot Perception and Navigation in Logistics and Inspection IROS 2024 Workshop*, 2024.
- [48] V. Pritzl, M. Vrba, Y. Stasinchuk, V. Krátky, J. Horyna, P. Štěpán, and M. Saska, "Drones guiding drones: Cooperative navigation of a less-equipped micro aerial vehicle in cluttered environments," in *IEEE/RSJ International Conference on Intelligent Robots and Systems (IROS)*, 2024.
- [49] M. Cihlářová, V. Pritzl, and M. Saska, "Cooperative indoor exploration leveraging a mixed-size uav team with heterogeneous sensors," in *IEEE International Conference on Automation Science and Engineering (CASE)*, 2024.
- [50] T. Baca, M. Petrlik, M. Vrba, V. Spurný, R. Penicka, D. Hert, and M. Saska, "The MRS UAV System: Pushing the Frontiers of Reproducible Research, Real-world Deployment, and Education with Autonomous Unmanned Aerial Vehicles," *Journal of Intelligent & Robotic Systems*, vol. 102, no. 1, p. 26, Apr. 2021.
- [51] S. Agarwal, K. Mierle, and T. C. S. Team, "Ceres Solver," Mar. 2022.
- [52] V. Pritzl, M. Vrba, C. Tortorici, R. Ashour, and M. Saska, "Adaptive estimation of uav altitude in complex indoor environments using degraded and time-delayed measurements with time-varying uncertainties," *Robotics and Autonomous Systems*, vol. 160, p. 104315, 2023.

- [53] E. Eade, "Process noise for gaussian random walks," 2017. [Online]. Available: https://ethaneade.com/process_noise_random_walk.pdf
- [54] J. Zhang and S. Singh, "LOAM: Lidar Odometry and Mapping in Real-time," in *Robotics: Science and Systems*, Jul. 2014, pp. 109–111.
- [55] T. Qin, P. Li, and S. Shen, "VINS-Mono: A Robust and Versatile Monocular Visual-Inertial State Estimator," *IEEE Transactions on Robotics*, vol. 34, no. 4, pp. 1004–1020, Aug. 2018.
- [56] D. Hert, T. Baca, P. Petracek, V. Kratky, R. Penicka, V. Spurny, M. Petrlik, M. Vrba, D. Zaitlik, P. Stoudek, V. Walter, P. Stepan, J. Horyna, V. Pritzl, M. Sramek, A. Ahmad, G. Silano, D. Bonilla Licea, P. Stibinger, T. Nascimento, and M. Saska, "MRS Drone: A Modular Platform for Real-World Deployment of Aerial Multi-Robot Systems," *Journal of Intelligent & Robotic Systems*, vol. 108, pp. 1–34, July 2023.
- [57] Z. Zhang and D. Scaramuzza, "A Tutorial on Quantitative Trajectory Evaluation for Visual(-Inertial) Odometry," in *IEEE/RSJ International Conference on Intelligent Robots and Systems (IROS)*, Oct. 2018.
- [58] P. Geneva, K. Eickenhoff, W. Lee, Y. Yang, and G. Huang, "OpenVINS: A Research Platform for Visual-Inertial Estimation," in *IEEE International Conference on Robotics and Automation (ICRA)*, 2020.
- [59] Y. Bar-Shalom, X. Li, and T. Kirubarajan, *Estimation with Applications to Tracking and Navigation: Theory, Algorithms and Software*. John Wiley & Sons, Ltd, 2004.



VÁCLAV PRITZL received the M.Sc. degree in cybernetics and robotics from the Czech Technical University in Prague (CTU in Prague), Czech Republic, in 2020, where he is currently working toward the Ph.D. degree in cooperative multi-UAV navigation in GNSS-denied environments. He is a member of the Multi-robot Systems Lab, CTU in Prague. He has authored or coauthored ten publications in conferences and impacted journals with >200 citations indexed by Scholar and h-index 8.

His research interests include cooperative navigation of teams of UAVs in GNSS-denied environments. He was a member of CTU-UPENN-NYU team in the MBZIRC 2020.



MATOUŠ VRBA received the Ph.D. degree in detection and localization for autonomous aerial vehicles from the Czech Technical University in Prague (CTU in Prague), Czech Republic, in 2024. Since 2018, he is a member of the Multi-robot Systems Lab, CTU Prague. He has authored or coauthored 15 publications in conferences and impacted journals with >700 citations indexed by Scholar and h-index 13. His research interests include machine perception methods for marker-less

mutual localization of UAVs. He was a Member of the CTU-UPENN-NYU team in the MBZIRC 2020 and the CTU-CRAS-NORLAB team in the DARPA SubT competition.



PETR ŠTĚPÁN received the Ph.D. degree in sensor fusion for mapping from the Czech Technical University in Prague (CTU Prague), Prague, Czech Republic, in 2002. He is currently with the Multi-Robot Systems lab, CTU Prague, where he focuses on sensor fusion, mapping, localization, and planning for unmanned aerial vehicles. He has also been involved in industrial projects and the H2020 AerialCore project. He is a coauthor of >40 publications in conferences and impacted journals

with >700 citations indexed by Scholar and h-index 11. He was a member of CTU-UPenn-UoL and CTU-UPENN-NYU teams in the MBZIRC 2017 and MBZIRC 2020 robotic competitions in Abu Dhabi.



MARTIN SASKA received the Ph.D. degree in trajectory planning and optimal control for formations of autonomous robots from the University of Wuerzburg, Wuerzburg, Germany, in 2010, within the Ph.D. program of Elite Network of Bavaria. He founded and heads the Multi-robot Systems group at the Czech Technical University in Prague with more than 40 researchers. He was a Visiting Scholar with the University of Illinois at Urbana-Champaign, Champaign, IL, USA, and with the

University of Pennsylvania, Philadelphia, PA, USA. He has authored or coauthored >200 publications in conferences and impacted journals, including IJRR, AURO, JFR, ASC, EJC, with >7700 citations indexed by Scholar and h-index 51. His team won multiple robotic challenges in MBZIRC 2017, MBZIRC 2020, and DARPA SubT competitions.

...